Li, S., Moreno, M., Bedford, J., Rosenau, M., Heidbach, O., Melnick, D., Oncken, O. (2017): Postseismic uplift of the Andes following the 2010 Maule earthquake: Implications for mantle rheology. - *Geophysical Research Letters*, *44*, 4, pp. 1768—1776.

DOI: http://doi.org/10.1002/2016GL071995

AGU PUBLICATIONS

Geophysical Research Letters

RESEARCH LETTER
10.1002/2016GL071995

**Key Points:**
- Uplift in the Andes and subsidence in the hinterland are observed in the 6 years following the 2010 Maule earthquake
- A geodetic data-driven modeling strategy is used to infer a heterogeneous viscosity distribution in the subcontinental mantle
- Viscosity distribution correlates with the first-order thermomechanical transition from volcanic arc to craton area

**Supporting Information:**
- Supporting Information S1

**Correspondence to:**
S. Li,
shaoyang.li@gfz-potsdam.de

**Citation:**
Li, S., M. Moreno, J. Bedford, M. Rosenau, O. Heidbach, D. Melnick, and O. Oncken (2017), Postseismic uplift of the Andes following the 2010 Maule earthquake: Implications for mantle rheology, *Geophys. Res. Lett.*, *44*, 1768–1776, doi:10.1002/2016GL071995.

Received 30 NOV 2016
Accepted 15 FEB 2017
Accepted article online 18 FEB 2017
Published online 25 FEB 2017



# Postseismic uplift of the Andes following the 2010 Maule earthquake: Implications for mantle rheology

**Shaoyang Li[1], Marcos Moreno[1], Jonathan Bedford[1], Matthias Rosenau[1], Oliver Heidbach[1], Daniel Melnick[2,3], and Onno Oncken[1]**

[1]Helmholtz Centre Potsdam, GFZ German Research Centre for Geosciences, Potsdam, Germany, [2]Institut für Erd-und Umweltwissenschaften, Universität Potsdam, Potsdam, Germany, [3]Instituto de Ciencias de la Tierra, TAQUACH, Universidad Austral de Chile, Valdivia, Chile

**Abstract** Postseismic surface deformation associated with great subduction earthquakes is controlled by asthenosphere rheology, frictional properties of the fault, and structural complexity. Here by modeling GPS displacements in the 6 years following the 2010 $M_w$ 8.8 Maule earthquake in Chile, we investigate the impact of heterogeneous viscosity distribution in the South American subcontinental asthenosphere on the 3-D postseismic deformation pattern. The observed postseismic deformation is characterized by flexure of the South America plate with peak uplift in the Andean mountain range and subsidence in the hinterland. We find that, at the time scale of observation, over 2 orders of magnitude gradual increase in asthenosphere viscosity from the arc area toward the cratonic hinterland is needed to jointly explain horizontal and vertical displacements. Our findings present an efficient method to estimate spatial variations of viscosity, which clearly improves the fitting to the vertical signal of deformation. Lateral changes in asthenosphere viscosity can be correlated with the thermomechanical transition from weak subvolcanic arc mantle to strong subcratonic mantle, thus suggesting a stationary heterogeneous viscosity structure. However, we cannot rule out a transient viscosity structure (e.g., power law rheology) with the short time span of observation.

## 1. Introduction

The relaxation process following large earthquakes provides the opportunity to constrain rheological properties of the Earth. The rupture of a great megathrust earthquake ($>M_w$ 8) imposes significant quasi-instantaneous stress perturbation (approximately several MPa) in the system, the relaxation of which is manifested by hour to decadal scale transient postseismic surface deformation. Short- to long-term postseismic relaxation processes occur in the near- and far field including afterslip [e.g., *Avouac*, 2015; *Marone et al.*, 1991], poroelastic rebound [e.g., *Hu et al.*, 2014; *Peltzer et al.*, 1996], and viscoelastic relaxation of the asthenosphere [e.g., *Sun et al.*, 2014; *Wang et al.*, 2012]. Contemporaneously, reloading due to relocking of the plate interface occurs [e.g., *Bedford et al.*, 2016; *Remy et al.*, 2016]. Deformation patterns of these processes overlap significantly around the fault rupture zone (near field) [*Jonsson et al.*, 2003; *Pollitz et al.*, 1998]. In the far field, viscoelastic relaxation dominates the postseismic deformation field and can be separated from afterslip and poroelastic rebound due to its longer wavelength and relaxation time [e.g., *Freed et al.*, 2007; *Freed et al.*, 2012].

The South American continent provides the rare opportunity to probe the viscoelastic behavior of the subcontinental mantle because of its active margin with high convergence rate (>6 cm/yr) and its large spatial extent in the "hinterland" of the subduction zone (i.e., the area encompassing the volcanic arc, back arc, and continental platform). Continuous Global Positioning System (GPS) coverage all over the South American continent has been established by scientific programs in the last decade [e.g., *Schurr et al.*, 2009] and virtually set ups a "large aperture lens" into the Earth. The $M_w$ 8.8 27 February 2010 Maule Chile earthquake was the first great earthquake captured by a large and extensive GPS network allowing to study postseismic processes at plate scale.

We here use 6 years of continuous GPS surface deformation observation in combination with finite element modeling to constrain viscoelastic properties of the South American subcontinental mantle. In contrast to other model approaches which implement a priori set rheological or structural complexity, we present a data-driven method for estimating first-order viscosity heterogeneity in a simple Maxwell viscoelastic body representing the subcontinental asthenosphere. By exploring the forward viscoelastic models with and

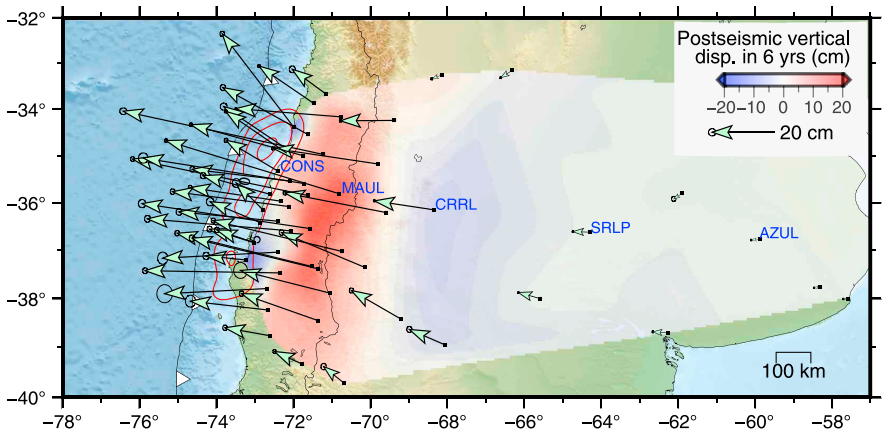


**Figure 1.** GPS measurements after the 2010 $M_w$ 8.8 Maule earthquake. The cumulative static displacements for the first 6 years following the Maule earthquake retrieved from cGPS stations. The red contours are coseismic slip distribution from *Moreno et al.* [2012] in meters. The blue characters denote the stations plotted in Figure S1.

without such lateral viscosity heterogeneity, we investigate its role on the 3-D, particularly the vertical, surface deformation signal. Finally, we discuss the implication of the inferred viscosity structure in terms of the mantle rheology.

## 2. Postseismic GPS Observations

The landward side of the Maule rupture zone is very well covered by GPS stations, monitoring 3-D surface motions from the coastline, at only some 100 km from the trench, up to about 1500 km from the trench (Figure 1). In this study, we focus on the postseismic response of the Maule event and hence only choose seaward-moving stations [e.g., *Wang et al.*, 2012]. We retrieve the cumulative postseismic displacements up to 6 years after the earthquake by using daily continuous GPS (cGPS) time series processed at the Nevada Geodetic Laboratory (Nevada Bureau of Mines and Geology, University of Nevada, U.S., http://geodesy.unr.edu/index.php, last accessed on 02/02/2016). In order to increase the reliability of GPS displacement retrievement, we only use the stations with sufficient temporal coverage (i.e., more than 3–4 year continuous observations) and find 55 stations that meet our temporal coverage criteria well distributed in both the near and very far fields. Details of GPS time series analysis refer to Text S1 in the supporting information.

Figure 1 shows the archetypical postseismic surface deformation of a great subduction earthquake as the Maule earthquake accumulated during the 6 years after the event. All stations show seaward horizontal motion with the stations near the rupture area diverging and the stations in the back arc converging toward the rupture zone, forming clockwise and anticlockwise rotations near the north and south edges of the rupture zone, respectively. Vertically, the stations show significant uplift in the mountain range and gentle subsidence in the back arc, forming a long wavelength lithospheric flexure pattern.

Since this study is focused on investigating the lateral viscosity structure and its impact on the far-field postseismic deformation, we do not include the near-field stations $<$300 km trench distance (i.e., the fore-arc area) in the analysis. The near field may be strongly affected by afterslip, poroelastic effects, and relocking of the plate interface, as demonstrated by previous postseismic studies of Maule earthquake [e.g., *Bedford et al.*, 2016; *Bedford et al.*, 2013; *Klein et al.*, 2016; *Lin et al.*, 2013]. Distribution of the stations as neglected versus selected for the analysis is shown in Figure S2 in the supporting information.

## 3. Viscoelastic Modeling Strategy

### 3.1. Finite Element Model Setups

We generate continental-scale 3-D finite element models for postseismic viscoelastic modeling and consider the crust and lithospheric mantle as an elastic body and the asthenosphere mantle as a Maxwell viscoelastic body. Hence, the structure of our 3-D model consists of four bodies (Figure S3), namely, (1) continental plate (mean thickness 45 km), (2) viscoelastic continental mantle, (3) oceanic plate (mean thickness 30 km), and (4) viscoelastic oceanic mantle. All numerical simulations in this study are solved with the 3-D finite element

software PyLith [*Aagaard et al.*, 2013]. The 3-D geometry of our model incorporates the geometry of the subduction slab and the continental Moho (Figure S3a, [*Contreras-Reyes and Osses*, 2010; *Hayes et al.*, 2012; *Tassara and Echaurren*, 2012], following our previous studies of the south-central Chile area [e.g., *Moreno et al.*, 2012]. The material properties used in the modeling and their corresponding references are described in Table S2 in the supporting information. In order to minimize boundary effects, we set our model boundaries far away from our study area, especially in the east-west model extension, in which most horizontal deformation occurs. The model area is about 4000 km in the E-W direction, 2000 km in the N-S direction, and 400 km in the vertical direction (Figure S3a). The model mesh is shown in Figure S3b.

The postseismic motions are simulated by initially imposing a coseismic slip distribution (from *Moreno et al.*, [2012]) on the fault interface and then relaxing the viscoelastic mantle for the 6 year observation period. We assume that the viscoelastic relaxation of the system is mainly due to the coseismic rupture and hence neglect the viscoelastic relaxation of other processes (i.e., aftershocks, afterslip, and fault locking). The east and west boundaries and the base of the problem domain are fixed in all directions, while the north and south boundaries and the top of the problem domain have no constraints (free to move in all directions). Therefore, the surface deformations predicted by postseismic models are directly comparable to the used 3-D GPS data, which is defined with respect to a stable South American reference frame. Moreover, we assume the same viscosity of the continental and oceanic mantle in the homogeneous model and neglect the geothermally controlled vertical viscosity variations in order to decrease the free modeling parameters and focus on the first-order lateral viscosity variation.

In order to validate the coseismic elastic behavior in our finite element model setups, we forward model the slip and compare its predictions with published GPS data [*Moreno et al.*, 2012]. As shown in Figure S4, the predicted coseismic surface displacements agree with the GPS observations exceedingly well using the elastic predictions from our model with the *Moreno et al.* [2012] slip distribution.

### 3.2. Testing the Effects of Lateral Viscosity Changes on Postseismic Deformation

Inspired by the geodetically observed long-wavelength vertical deformation signal ("flexure"; Figure 1), we synthetically investigate the principal effects of laterally varying viscosity on the surface postseismic deformation pattern in the time window of 6 years following the earthquake. In its simplest form, this lateral variation can be represented by a model with a single mantle viscosity contrast in E-W direction (hereafter named the "heterogeneous model"). The model with lateral viscosity variation is compared to a model with a single viscosity ("homogeneous model"). For the heterogeneous model, a relatively low-viscosity domain is located beneath the fore arc and Andean mountain range (Figure 2). We analyze three models of this kind with a low viscosity reaching successively further into the continent: Model 1 including the fore arc (0–300 km from the trench), Model 2 including the fore arc and arc (0–400 km from the trench), and Model 3 including the fore arc, arc, and back arc (0–500 km from the trench), and examine the impact on the vertical and horizontal surface deformation signal.

The heterogeneous model results in a similar general horizontal deformation pattern to the homogeneous model, except that, for the heterogeneous model, the magnitude of the horizontal deformation increases on the trench side of the viscosity boundary and decreases on the other side (Figures 2a and 2c). However, the vertical deformation patterns from the heterogeneous models are markedly different from the model with the homogeneous viscosity distribution (Figures 2b and 2d). The vertical deformation decreases locally (Figure 2b) and results in a subsidence zone located almost directly above the viscosity boundary (Figure 2d). The modeling results thus indicate that a change from a low- to high-viscosity domain causes a localized extensional and subsiding zone around the viscosity boundary.

Furthermore, we test the influence of a more viscous zone sandwiched in-between two less viscous zones on surface deformation. This structure produces significant uplift around the boundary of high viscosity to low viscosity and subsidence around another boundary of low viscosity to high viscosity (Figure S5).

In conclusion, these model results indicate that the magnitudes of the observed horizontal deformation are potentially useful for the estimation of lateral viscosity changes. However, the sign of vertical deformation (i.e., uplifting or subsiding) is particularly diagnostic and thus potentially a direct indicator of the location of lateral viscosity heterogeneities. Based on the GPS observed deformation and the above synthetic modeling results, we propose a viscosity contrast in the back arc and explore a refinement model in section 3.4.

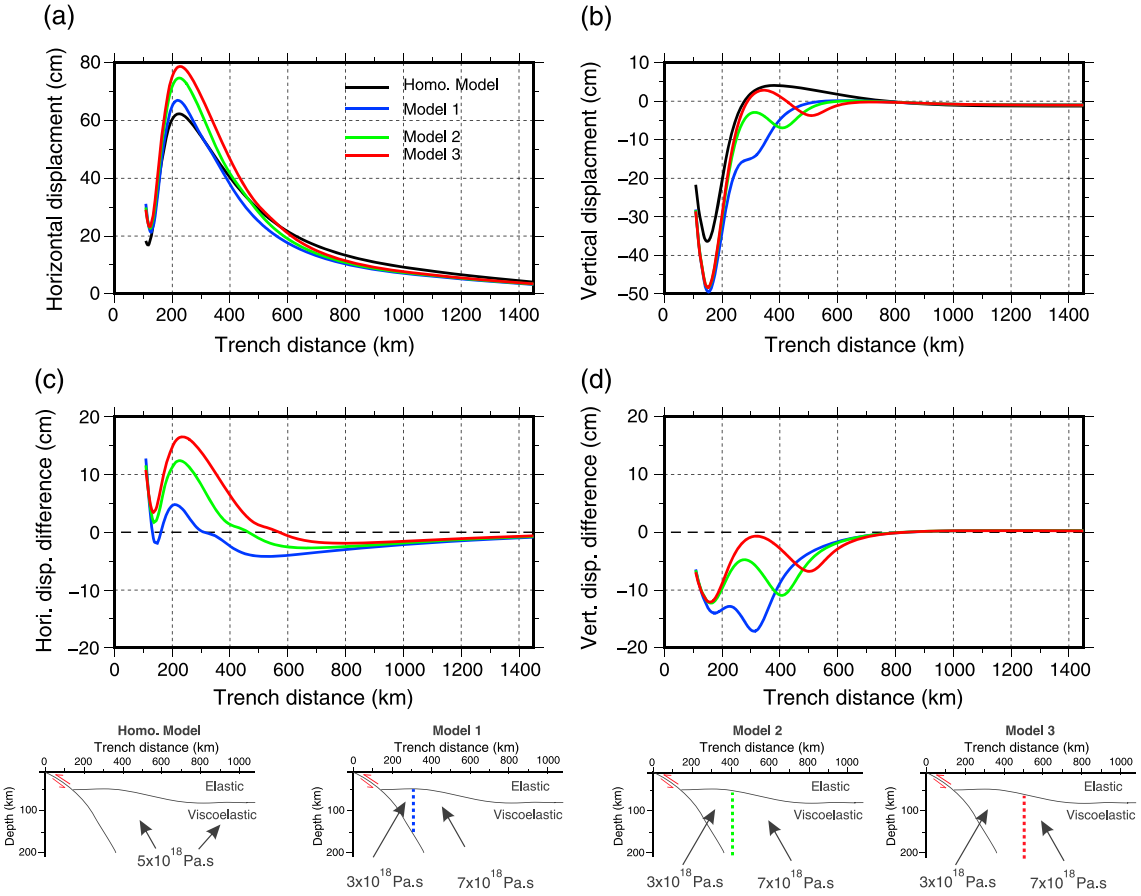


**Figure 2.** Results of synthetic models that test the influence of a single lateral mantle viscosity contrast on the surface deformation pattern. (a and b) The 6 year modeling displacements from different end-member models in horizontal and vertical directions, respectively. (c and d) Displacement differences between heterogeneous and homogeneous models in the horizontal and vertical directions, respectively. Small schematic plots below show the specified viscosity structure in the end-member forward models. The colorful dashed lines show the locations of the viscosity boundaries.

### 3.3. Estimating Lateral Variation of Viscosity

In order to map the potential viscosity heterogeneities, we develop a data-driven approach that initially constrains an optimal viscosity value at each GPS station. The viscosity estimation consists of two steps: (1) we repeatedly simulate the postseismic homogeneous viscoelastic model, each time varying the viscosity (for a range of viscosities between $10^{17}$ and $10^{21}$ Pa s) in the asthenosphere; (2) an optimal homogeneous viscosity is then determined at each individual station by selecting the homogeneous model that produces the lowest weighted root-mean-square (WRMS) misfit in fitting the cumulative displacement at this station. In parameterizing the optimal homogeneous viscosities, we fit the horizontal displacement and not the vertical at this stage because a model with homogeneous viscosity will always predict subsidence from the coastline to ~300 km trench distance (Figure S6). Figure S7 shows the viscosity as retrieved separately at all the GPS stations.

### 3.4. Designing Lateral Heterogeneous Viscoelastic Forward Models

In order to configure the 3-D heterogeneous viscoelastic forward models, we divide the viscoelastic mantle in space by projecting all the GPS stations vertically down to the mantle (Figure S8). All the finite elements closest to the projection are attributed the viscosity retrieved from the corresponding above GPS station. With different viscosity values estimated at different stations (method details in section 3.3; Figure S7), we construct a unified heterogeneous viscoelastic mantle in forward models.

Moreover, considering the synthetic modeling results (Figures 2 and S4) in section 3.2, we test whether the subsidence signal is due to a transition from low viscosity to high viscosity in the landward direction. Such a transition is consistent with the geophysical studies showing that the South American lithosphere

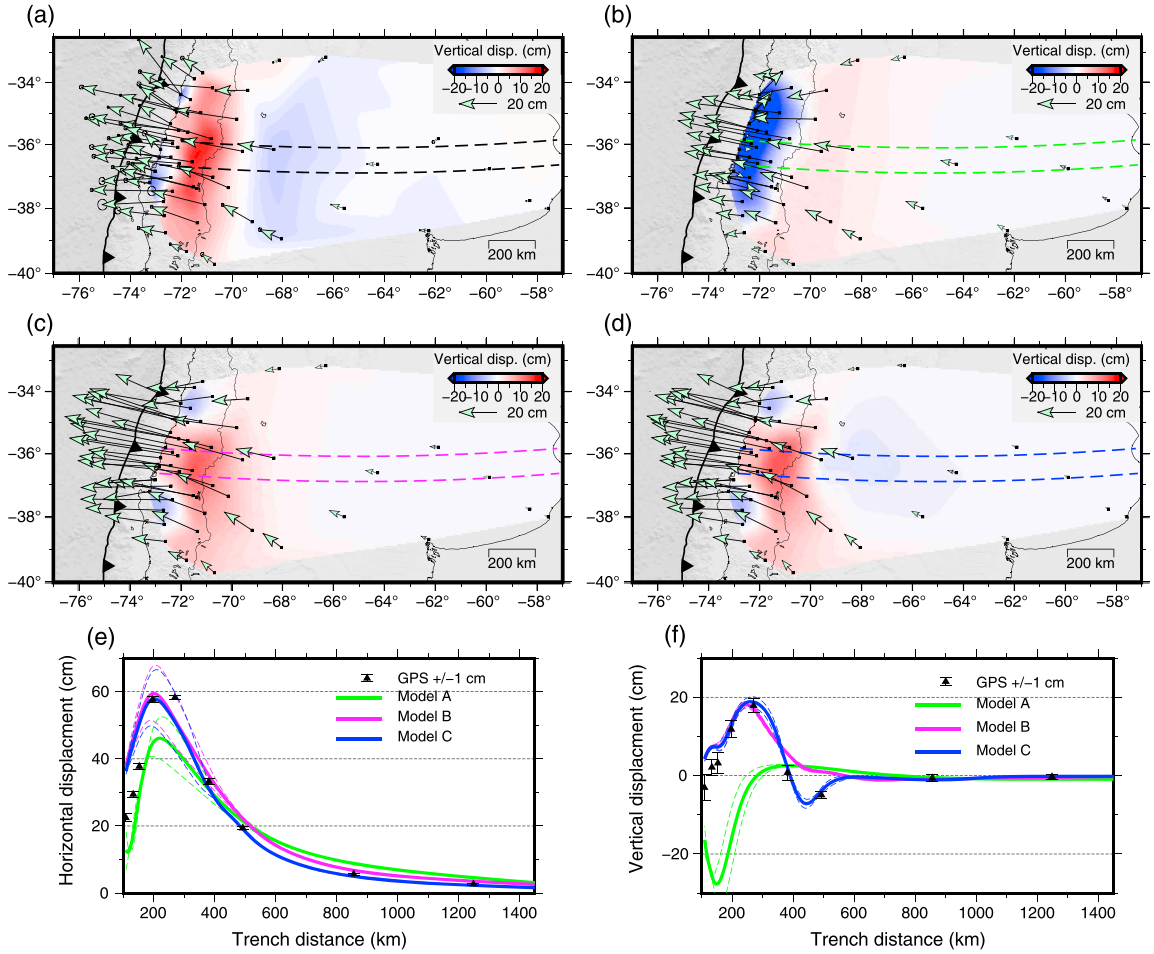


**Figure 3.** Comparison of deformation patterns from GPS observations and model predictions for Models A–C. (a) Cumulative GPS observations for the first 6 years of cumulative postseismic deformation same as Figure 1. (b–d) The first 6 years of postseismic predictions of surface deformation for Models A–C, respectively. (e and f) The comparisons of GPS observations and model predictions within the swath profile in horizontal and vertical directions, respectively. The dashed lines show the maximum and minimum values within the profile.

thickens and effective viscosities increase landward of the back-arc region due to the presence of the Argentina Craton (i.e., Río de la Plata Craton) [e.g., *Pérez-Gussinyé et al.*, 2008].

In all, we obtain three end-member forward models: (1) Model A: the best homogeneous viscoelastic model that can explain all the GPS displacements (i.e., the model has minimum overall WRMS, which has a mantle viscosity of $6.5 \times 10^{18}$ Pa s); (2) Model B: the unified heterogeneous viscoelastic model constructed from the determined viscosities at all the stations (i.e., Figure S7); and (3) Model C: identical lateral viscosity distribution to Model B except for distances greater than 700 km from the trench where we specify the viscosity as $10^{30}$ Pa s; i.e., we assume a purely elastic response of the subcratonic asthenosphere in the respective time scale of observations. In the following section, we present the results of these three end-member models in predicting the GPS observations.

## 4. Modeling Results

We explore the model predictions for the viscous relaxation of forward models (i.e., Models A–C) in response to the coseismic stress changes released in the first 6 years following the earthquake. Model A produces the horizontal surface deformation directed toward the coseismic rupture zone (Figure 3b), which is similar to the deformation pattern observed by GPS (Figure 3a). The modeled subsidence is localized in the zone above the downdip end of rupture between the Chilean coastline and the Chilean national boundary to Argentina (i.e., about 100 to 300 km trench distance), surrounded by a zone of broadly distributed modest uplift in the

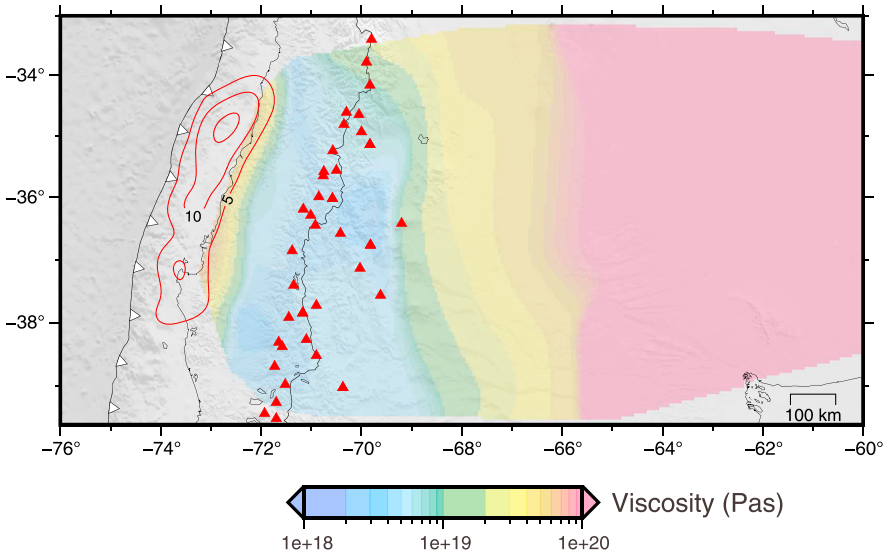


**Figure 4.** The optimal heterogeneous viscosity distribution inferred in this study. The gray background is shaded relief map of the Andean subduction zone. The red contours are coseismic slip distribution from *Moreno et al.* [2012] in meters. The red triangles indicate active volcanoes.

east. The vertical displacement pattern predicted by Model A is almost opposite to that of the GPS observation from 200 km trench distance to the far back-arc area (Figure 3a). In the area from 100 to 300 km, Model A predicts significant subsidence while the GPS data show strong uplift; in the area from 300 km to 800 km, Model A predicts gentle uplift while the GPS data measure modest subsidence (Figure 3e).

Models B and C produce a similar deformation pattern in both horizontal and vertical directions. In comparison to Model A, Models B and C predict a larger horizontal deformation gradient in the area from 200 to 400 km trench distance (Figures 3c and 3d). Notably, only Models B and C reproduce uplift of the Andean mountain range consistent with the GPS measurements and contrasting with that of Model A. Therefore, fitting the uplift signal in Andean mountain range requires the lateral viscosity heterogeneity involving relatively low mantle viscosity beneath the Andean mountains.

In comparison to Model B, Model C slightly improves the performance in horizontal deformation prediction in the area >500 km trench distance and significantly improves the back arc (from 400 to 700 km trench distance) subsidence prediction (Figures 3e and 3f).

We calculate the residuals of the three models in fitting the GPS observations (Figure S9). Model A has large residuals in the area from 200 to 600 km trench distance (approximately between −72° and −68°E) in both horizontal and vertical directions (Figure S9a), whereas both Models B and C perform much better in terms of the residuals (Figures S9b and S9c). Model C has the smaller residuals in vertical motion in comparison to Model B.

The optimal heterogeneous viscosity structure is therefore proposed in this study as the structure specified in Model C (Figure 4). The structure exhibits significant lateral viscosity variation characterized by a general increase toward the hinterland: from ~$10^{18}$ Pa s beneath the Andean mountain range (<400 km trench distance) to ~$10^{20}$ Pa s beneath the back-arc region (<700 km trench distance) and a sharp increase to $10^{30}$ Pa s beneath the South American cratonic mantle (>700 km trench distance) at the time scale of postseismic observation. The viscosity pattern also shows a moderate lateral variation in the strike direction. The pattern is somewhat symmetric around the latitude of the Maule earthquake occurrence.

## 5. Discussion

### 5.1. Sensitivity Tests

In order to check how robust the model results are, we test the impact of the chosen boundary conditions, the thickness of the elastic upper crust, and the sensitivity of the results with our constructed viscosity structure. For the latter, we assumed in the construction of the forward heterogeneous models (i.e., Models B and C)

that each cumulative GPS displacement is most sensitive to the local viscosity value beneath the station, i.e., the retrieved viscosities are interpreted as the averaged effects of rheological heterogeneity and geometries at depth beneath each GPS station in the studied time window. We check this assumption and illuminate the applicability and limitations of our approach by testing how well our scheme can recover the specified viscosity distribution from the surface displacement predictions of the forward heterogeneous models. This test is similar to a checkerboard analysis. The results (Figure S10) show that, although our approach cannot fully resolve the specified viscosity structure in all detail, it achieves the recovery in the first order with error less than 1 order of viscosity magnitude at each station.

For the other two sensitivity tests, we checked the impact of fixed boundaries in the north and south and a reasonable variation of the elastic thickness. The changes of the boundary conditions show that, in the area of interest, the differences are close to zero and thus negligible; only toward the outer bounds of the model area are differences visible, but not larger than 2 cm. The change of the elastic thickness between 40 and 60 km (in order to study the trade-off between the determined viscosity structure and the assumed upper plate structure) has a small impact on the model results (Figure S6) but does not change the general finding that a lateral viscosity structure is probably of key importance to explain the vertical postseismic deformation signal.

### 5.2. Mantle Rheology

The optimal lateral viscosity structure determined in our study exhibits a low viscosity zone beneath the Andean mountain range and a high-viscosity, quasi-elastic (at the observation time scale) subcratonic mantle. Assuming that the proposed viscosity structure is stationary, we attribute the low and high viscosities to relatively high and low geothermal gradients, respectively. A high geotherm from the surface down into the mantle can be expected in the volcanic arc area [*Hamza and Muñoz*, 1996; *Springer*, 1999]. Here magma rises through the lithosphere from a source in the asthenospheric wedge where fluids liberated by metamorphic mineral reactions in subducted slab material trigger partial melting. Vice versa, the geotherm in the tectonically stable, thick cratonic lithosphere, and underlying mantle can be expected to reach a continental minimum.

Apart from the first-order thermomechanically controlled, stationary viscosity structure suggested here, alternative models of mantle rheology might apply. Especially, more complex or transient viscosity structures may be relevant. Transient viscosity structures include power law [*Freed and Burgmann*, 2004; *Kirby and Kronenberg*, 1987] and bi-viscous Burgers rheology [*Klein et al.*, 2016; *Peltier et al.*, 1981; *Pollitz et al.*, 2008; *Wang et al.*, 2012]. In transient viscosity models the viscoelastic structure is time-dependent; i.e., viscosities change as a function of time and/or stress. Whether such a complex rheology is required to model the Maule 2010 earthquake postseismic response accurately cannot be judged on the basis of only 6 year observations. As we show, our simple model explains the observations sufficiently well. However, the general trend of decreasing viscosity toward the rupture as shown here is consistent with such a transient viscosity model. Especially, the indicated along-strike symmetry of the viscosity structure might be easier to explain with a stress-dependent viscosity (power law rheology) than with a stationary mechanical structure. More complex viscous structures may include a subduction channel, a weak layer below the elastic part of the oceanic plate, and also a depth or temperature dependent viscosity structure [e.g., *Hu et al.*, 2015; *Klein et al.*, 2016; *Muto et al.*, 2016; *Sun and Wang*, 2015; *Sun et al.*, 2014; *Wiseman et al.*, 2015]. For instance, the uplift pattern over the Cordillera following Maule earthquake may be equally explained by a subduction channel extending from 55 to 135 km depth [*Klein et al.*, 2016].

However, given the nonuniqueness of solutions to this problem, we here propose to use the simplest model and revisit the problem in the future when the relaxation process matured significantly to allow distinguishing between stationary and transient viscosity structures.

## 6. Conclusion

The postseismic surface deformation pattern following a large megathrust earthquake allows probing the viscoelastic rheology of the asthenospheric mantle. We here have considered 6 year GPS cumulative displacements after the 2010 $M_w$ 8.8 Maule earthquake to constrain the lateral viscosity structure in a Maxwell-type mantle underneath South America between 33°S and 40°S latitude. Surface deformation is characterized by seaward converging-diverging pattern of horizontal displacement along with long wavelength

lithospheric "flexure", i.e., uplift of Andean mountain range and subsidence of the back arc. A homogenous viscosity structure is rejected based on the sign of the vertical deformation. A heterogeneous model with generally decreasing viscosity toward the rupture area reproduces best the 3-D GPS observations. The heterogeneous viscosity structure shows significant lateral variation: at distances up to 700 km from the trench, the mantle viscosity gradually increases landward of the back-arc region from ~$10^{18}$ to ~$10^{20}$ Pa s. In the very far field (>700 km trench distance), the mantle may behave almost purely elastically at the time scale of observation. We correlate the inferred stationary viscosity distribution to first-order thermomechanical provinces, i.e., the relatively hot and weak fore-arc-arc region and the relatively cold and strong subcratonic area. However, both a more complex stationary structure and more complex rheologies imposing a transient viscosity structure may explain the observed deformation equally well.

**Acknowledgments**

Shaoyang Li gratefully acknowledges the scholarship granted to him by the China Scholarships Council (201206040055). Shaoyang Li is a member of the Helmholtz graduate research school GeoSim. Marcos Moreno and Jonathan Bedford have been supported by the PESCADOS project. The postseismic displacements are derived from the daily time series from Nevada Geodetic Laboratory (http://geodesy.unr.edu/index.php). Postseismic modeling results for this paper are available by contacting Shaoyang Li at shaoyang.li@gfz-potsdam.de. The authors would like to thank the developers of the open-source PyLith software for their ongoing dedication to the software development and generous technical support. We would like to thank Roland Burgmann and Romain Jolivet for the constructive review of an earlier version of the paper and Kelin Wang for the comments of an internal review. We would like to thank two anonymous reviewers and Editor Andrew Newman for their invaluable comments and suggestions. Some of the figures in this paper were created with GMT software [*Wessel and Smith*, 1998].

## References

Aagaard, B. T., M. G. Knepley, and C. A. Williams (2013), A domain decomposition approach to implementing fault slip in finite-element models of quasi-static and dynamic crustal deformation, *J. Geophys. Res. Solid Earth*, *118*, 3059–3079, doi:10.1002/jgrb.50217.

Avouac, J.-P. (2015), From geodetic imaging of seismic and aseismic fault slip to dynamic modeling of the seismic cycle, *Annu. Rev. Earth Planet. Sci.*, *43*(1), 233–271.

Bedford, J., M. Moreno, J. C. Baez, D. Lange, F. Tilmann, M. Rosenau, O. Heidbach, O. Oncken, M. Bartsch, and A. Rietbrock (2013), A high-resolution, time-variable afterslip model for the 2010 Maule $M_w$ = 8.8, Chile megathrust earthquake, *Earth Planet. Sci. Lett.*, *383*, 26–36.

Bedford, J., M. Moreno, S. Li, O. Oncken, J. C. Baez, M. Bevis, O. Heidbach, and D. Lange (2016), Separating rapid relocking, afterslip, and viscoelastic relaxation: An application of the postseismic straightening method to the Maule 2010 cGPS, *J. Geophys. Res. Solid Earth*, *121*, 7618–7638, doi:10.1002/2016JB013093.

Contreras-Reyes, E., and A. Osses (2010), Lithospheric flexure modelling seaward of the Chile trench: Implications for oceanic plate weakening in the trench outer rise region, *Geophys. J. Int.*, *182*(1), 97–112.

Freed, A. M., and R. Burgmann (2004), Evidence of power-law flow in the Mojave desert mantle, *Nature*, *430*(6999), 548–551.

Freed, A. M., R. Burgmann, and T. Herring (2007), Far-reaching transient motions after Mojave earthquakes require broad mantle flow beneath a strong crust, *Geophys. Res. Lett.*, *34*, L19302, doi:10.1029/2007GL030959.

Freed, A. M., G. Hirth, and M. D. Behn (2012), Using short-term postseismic displacements to infer the ambient deformation conditions of the upper mantle, *J. Geophys. Res.*, *117*, B01409, doi:10.1029/2011JB008562.

Hamza, V. M., and M. Muñoz (1996), Heat flow map of South America, *Geothermics*, *25*(6), 599–646.

Hayes, G. P., D. J. Wald, and R. L. Johnson (2012), Slab1.0: A three-dimensional model of global subduction zone geometries, *J. Geophys. Res.*, *117*, B01302, doi:10.1029/2011JB008524.

Hu, Y., R. Burgmann, J. Freymueller, P. Banerjee, and K. Wang (2014), Contributions of poroelastic rebound and a weak volcanic arc to the postseismic deformation of the 2011 Tohoku earthquake, *Earth Planets Space*, *66*(1), 1–10.

Hu, Y., R. Bürgmann, N. Uchida, P. Banerjee, and J. T. Freymueller (2015), Stress-driven relaxation of heterogeneous upper mantle and time-dependent afterslip following the 2011 Tohoku earthquake, *J. Geophys. Res. Solid Earth*, *121*, 385–411, doi:10.1002/2015JB012508.

Jonsson, S., P. Segall, R. Pedersen, and G. Bjornsson (2003), Post-earthquake ground movements correlated to pore-pressure transients, *Nature*, *424*(6945), 179–183.

Kirby, S. H., and A. K. Kronenberg (1987), Rheology of the lithosphere: Selected topics, *Rev. Geophys.*, *25*, 1219–1244, doi:10.1029/RG025i006p01219.

Klein, E., L. Fleitout, C. Vigny, and J. D. Garaud (2016), Afterslip and viscoelastic relaxation model inferred from the large-scale post-seismic deformation following the 2010 $M_w$ 8.8 Maule earthquake (Chile), *Geophys. J. Int.*, *205*(3), 1455–1472.

Lin, Y. N., et al. (2013), Coseismic and postseismic slip associated with the 2010 Maule Earthquake, Chile: Characterizing the Arauco Peninsula barrier effect, *J. Geophys. Res. Solid Earth*, *118*, 3142–3159, doi:10.1002/jgrb.50207.

Marone, C., C. Scholtz, and R. Bilham (1991), On the mechanics of earthquake afterslip, *J. Geophys. Res.*, *96*(B5), 8441–8452, doi:10.1029/91JB00275.

Moreno, M., et al. (2012), Toward understanding tectonic control on the $M_w$ 8.8 2010 Maule Chile earthquake, *Earth Planet. Sci. Lett.*, *321–322*, 152–165.

Muto, J., B. Shibazaki, T. Iinuma, Y. Ito, Y. Ohta, S. Miura, and Y. Nakai (2016), Heterogeneous rheology controlled postseismic deformation of the 2011 Tohoku-Oki earthquake, *Geophys. Res. Lett.*, *43*, 4971–4978, doi:10.1002/2016GL068113.

Peltier, W. R., P. Wu, and D. A. Yuen (1981), The viscosities of the Earth's mantle, in *Anelasticity in the Earth*, edited by F. D. Stacey, M. S. Paterson, and A. Nicolas, pp. 59–77, AGU, Washington, D. C.

Peltzer, G., P. Rosen, F. Rogez, and K. Hudnut (1996), Postseismic rebound in fault step-overs caused by pore fluid flow, *Science*, *273*, 1202–1204.

Pérez-Gussinyé, M., A. R. Lowry, J. Phipps Morgan, and A. Tassara (2008), Effective elastic thickness variations along the Andean margin and their relationship to subduction geometry, *Geochem. Geophys. Geosyst.*, *9*, Q02003, doi:10.1029/2007GC001786.

Pollitz, F. F., R. Burgmann, and P. Segall (1998), Joint estimation of afterslip rate and postseismic relaxation following the 1989 Loma Prieta earthquake, *J. Geophys. Res.*, *103*(B11), 26,975–26,992, doi:10.1029/98JB01554.

Pollitz, F., P. Banerjee, K. Grijalva, B. Nagarajan, and R. Burgmann (2008), Effect of 3-D viscoelastic structure on post-seismic relaxation from the 2004 M = 9.2 Sumatra earthquake, *Geophys. J. Int.*, *173*, 189–204.

Remy, D., H. Perfettini, N. Cotte, J. P. Avouac, M. Chlieh, F. Bondoux, A. Sladen, H. Tavera, and A. Socquet (2016), Postseismic relocking of the subduction megathrust following the 2007 Pisco, Peru, earthquake, *J. Geophys. Res. Solid Earth*, *121*, 3978–3995, doi:10.1002/2015JB012417.

Schurr, B., A. Asch, F. Sodoudi, A. Manzanares, O. Ritter, J. Klotz, G. Chong-Diaz, S. Barrientos, J.-P. Villotte, and O. Oncken (2009), The International Plate Boundary Observatory Chile (IPOC) in the northern Chile seismic gap paper presented at EGU General Assembly Conf. Abstr.

Springer, M. (1999), Interpretation of heat-flow density in the Central Andes, *Tectonophysics*, *306*(3–4), 377–395.

Sun, T., and K. Wang (2015), Viscoelastic relaxation following subduction earthquakes and its effects on afterslip determination, *J. Geophys. Res. Solid Earth*, *120*, 1329–1344, doi:10.1002/2014JB011707.

Sun, T., et al. (2014), Prevalence of viscoelastic relaxation after the 2011 Tohoku-oki earthquake, *Nature*, *514*(7520), 84–87.
Tassara, A., and A. Echaurren (2012), Anatomy of the Andean subduction zone: Three-dimensional density model upgraded and compared against global-scale models, *Geophys. J. Int.*, *189*(1), 161–168.
Wang, K., Y. Hu, and J. He (2012), Deformation cycles of subduction earthquakes in a viscoelastic Earth, *Nature*, *484*(7394), 327–332.
Wessel, P., and W. H. F. Smith (1998), New, improved version of the Generic Mapping Tools released, *Eos Trans. AGU*, *79*, 579.
Wiseman, K., R. Bürgmann, A. M. Freed, and P. Banerjee (2015), Viscoelastic relaxation in a heterogeneous Earth following the 2004 Sumatra-Andaman earthquake, *Earth Planet. Sci. Lett.*, *431*, 308–317.